

# Numerical simulation and experimental investigation of arc based additive manufacturing assisted with external longitudinal static magnetic field

X.M. Zhou\*, H.O. Zhang\*†, G.L. Wang\*\* , L.Y. Liang\*\* , Y.H. Fu\*\* , X W Bai\* and X.P Wang\*

\*State Key Laboratory of Digital Manufacturing Equipment and Technology, Huazhong University of Science and Technology, Wuhan 430074, PR China

\*\*State Key Laboratory of Materials Processing and Die & Mould Technology, Huazhong University of Science and Technology, Wuhan 430074, PR China

REVIEWED

## Abstract

This paper proposes a new arc based additive manufacturing method assisted with external longitudinal static magnetic field. An electromagnetic coupling numerical model has been established, which consists of droplet impingement, heat transfer and dynamics of molten pool. Comparing the simulation results between normal deposition and external longitudinal magnetic field assisted deposition, it shows that the external longitudinal static magnetic field induces the tangential stirring force in molten pool and drives the molten metal moving to the edge of the pool. This can reduce the temperature gradient in forming region. Furthermore, the related comparison experiments of single-bead deposition and multi-beads overlapping deposition are performed, it was found that the tangential stirring force can reduce the height of single-bead as well as increase the width of single-bead. The experimental results are in accordance with the simulation results. The changing of morphology of the bead is beneficial to multi-beads overlapping and capable of improving the surface accuracy for arc based additive manufacturing parts.

## Introduction

Arc based additive manufacturing (AAM) is a wire and arc welding based additive manufacturing (AM) technology which has high energy efficiency [1] and deposition rate [2] comparing with laser or electron beam deposition AM technology. In AAM process, components are fabricated by overlapping weld beads in one layer and deposition of materials layer-by-layer in height direction, however, it is easy to introduce geometric error due to the accuracy limitation of Gas Metal Arc Welding (GMAW) (or Gas Tungsten Arc Welding, GTAW) and cumulative error in the process of overlapping. Several researches have been devoted to improve surface accuracy for arc welding based AM. Xiong et al. [3] established a model of bead section profile and overlapping beads with experimental validation for robotic GMAW-based AM, and obtained smooth surface with no defect by determined optimum model for single bead section. Later, Xiong et al. [4] developed a passive vision sensor system to monitor the nozzle to the top surface distance (NTSD) in arc welding based AM, and designed an adaptive control system to keep the NTSD constant by moving the working flat and adjusting the deposition rate on next deposition layer. These strategies can improve process stability and obtain smooth thin-walled parts. Ding et al. [5] built a single weld bead model through various curve fitting methods. Then they established a tangent overlapping model (TOM) and presented a concept of critical centre distance for stable multi-bead overlapping processes. The multi-bead and multi-layer deposition experiment indicated that the proposed TOM is better in geometry accuracy and material efficiency than traditional flat-top overlapping model (FOM).

The longitudinal magnetic field has been widely employed for electromagnetic assisted arc welding. Malinowski-Brodnicka et al. [6] investigated the effect of longitudinal electromagnetic stirring on austenitic stainless steel GTAW by experiments. It was found that an asymmetric weld bead was formed in the case of a constant magnetic field, when an alternating field was applied, a symmetric bead was formed. The increasing of field strength could result in increasing of weld width and decreasing of penetration. Simultaneously, the application of an alternating magnetic field could lead to grain refining on macro scale as well as micro scale. The changing of weld bead shape and metal structure were interpreted in terms of arc expansion, dendrite fragmentation, mixing of the liquid weld metal in the vicinity of the solidification. Chang et al. [7], Jiang et al.

[8] and Luo et al. [9] conducted an experiment of GMAW assisted with an external longitudinal magnetic field and found that the longitudinal magnetic field could improve the characteristics of arc plasma and metal transfer, such as reduction of spatter in certain welding conditions. Chang et al. [10] studied the impact of the synchronous longitudinal electromagnetic field including low-frequency(5-25Hz) and high-frequency magnetic fields(500-2000Hz) on short-circuit GMAW by multiple sets of comparative experiments, and found that all these two kinds of magnetic fields could improve the frequency of metal transfer and reduce the spatter.

To date, the studies of external magnetic field assisted arc welding or weld-based AM are mainly focusing on experimental study. Although the information obtained through experimental observations is very useful, it is difficult to use experimental methods to reveal underlying mechanisms due to high-temperature and transient during the arc welding. Numerical simulation provides an alternative way to obtain insightful physical phenomena. Ushio and Wu [11] built a three-dimensional modeling of heat and fluid flow in a moving gas metal arc weld pool. CAO et al. [12] developed a 3-D transient numerical model of gas metal arc (GMA) weld pools with free surface and droplet impact effects by considering not only the heat transfer and fluid flow, then simulated weld bead geometries were in good agreement with experimental measurements. Hu [13] and Rao [14] developed a uniform model covering arc droplet formation, detachment, transfer, impingement and weld pool dynamics. Later, Hu [15] and Rao [16] built a three-dimensional transient model of droplet impingement and weld pool dynamics, and investigated the influence of metal transport phenomena on the formation of ripples. Chang et al. [17] established a finite element model analysis on temperature field and stress field during submerged-arc welding to study the effects on weld bead formation by using longitudinal magnetic field of low-frequency. It was shown that a molten pool with a wider weld face and a lower penetration could be obtained and by the control of longitudinal magnetic field of low-frequency. Bai et al. [18] presented an induction heating assisted weld-based additive manufacturing process, and developed a coupling analysis FEM model of induction and arc heat. Then induction preheating and postheating on residual stress state are analyzed in comparative simulations. But the simulation model of Chang [17] and Bai [18] didn't include the weld pool dynamics. Luo et al.[19] utilized a probe to measure the distribution of arc current density with an additional longitudinal magnetic field and developed a model for the fluid flow in the weld pool for the control process, which was based on experiments using LD10CS aluminum alloy. The influences of the additional longitudinal magnetic field and other factors are discussed. Yin et al. [20] established a 3D numerical model containing the welding arc and the weld pool for gas tungsten arc welding (GTAW) with applied axial magnetic fields. The distribution of temperature, heat flux, current density and pressure on the anode surface becomes double-peaked while the applied axial magnetic fields were applied. The fluid in the centre areas rotates in an opposite direction to that in the outer regions. But this model does not include the free surface of weld pool.

In this paper, a new arc based additive manufacturing method assisted with external longitudinal static magnetic field is proposed, and a separation numerical model is developed for metal transfer and weld pool dynamics. The schematic of longitudinal magnetic field assisted AAM is shown in Fig.1. The detailed comparative analyses of temperature, velocity, and electromagnetic force are performed, and the simulation results are associated with the morphology of weld bead. Then the single-bead deposition and multi-beads overlapping experiments are performed, and the effect of the external longitudinal static magnetic field on the surface quality and dimensional accuracy of the AAM parts are discussed.

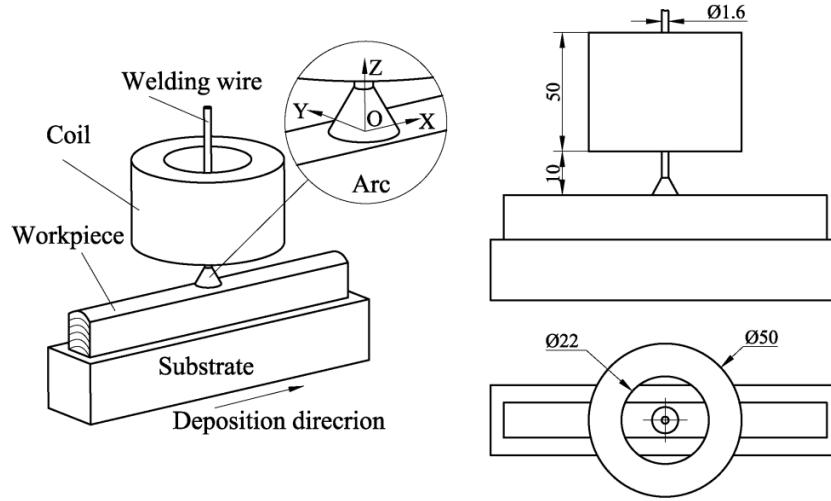


Fig. 1. A schematic representation of longitudinal magnetic field assisted AAM

## Mathematical models

### 1. Governing equations

The governing equations of heat and mass transfer are as following:

Mass continuum equation:

$$\frac{\partial}{\partial t}(\rho) + \nabla \cdot (\rho \mathbf{V}) = 0 \quad (1)$$

Momentum conservation equation:

$$\frac{\partial}{\partial t}(\rho \mathbf{V}) + \nabla \cdot (\rho \mathbf{V} \mathbf{V}) = -\nabla p + \nabla \cdot (\mu \nabla \mathbf{V}) + F_b + F_{arc} + F_{st} + F_{ms} + F_{drag} + F_{mag} \quad (2)$$

Energy conservation equation:

$$\frac{\partial}{\partial t}(\rho h) + \nabla \cdot (\mathbf{V} \rho h) = \nabla \cdot (k \nabla T) + S_{arc} + S_{drop} \quad (3)$$

In the above equations,  $\rho$  is density,  $\mathbf{V}$  is velocity vector,  $p$  is pressure, and  $\mu$  is viscosity, and  $h$  is enthalpy. The other items are source item and will be given as following.

#### a) Source item of mass

In this paper, the droplet is considered generating at a certain frequency and injecting to molten pool. The source item of mass can be written as,

$$S_{mass} = \frac{\rho_l}{\Delta t} \quad (4)$$

where  $\rho_l$  is density of liquid metal,  $\Delta t$  is droplet generation time.

#### b) Source item of momentum

The item  $F_b$  is buoyancy which can be calculated by Boussinesq approximation (Eq.(5)), where  $\rho_0$  is the (constant) density of the flow,  $T_0$  is the reference temperature, and  $\beta$  is the thermal expansion coefficient.

$$F_b = (\rho - \rho_0)g \approx \rho_0 \beta (T - T_0)g \quad (5)$$

In current study, the VOF method is employed to track the free surface.  $F(x,y,z,t)$  represents the volume of metallic phase per unit volume of fluid. The VOF equation is expressed as Eq.(444) . When  $F$  is between 0 and 1, it means that the cell is located at the free surface, and gradient direction of  $F$  that is normal direction of free surface.

$$\frac{dF}{dt} = \frac{\partial F}{\partial t} + (\mathbf{V} \cdot \nabla)F = 0 \quad (6)$$

The pressure of arc  $P_a$  is considered to be a Gaussian distribution [21]:

$$p_a = P_{\max} \exp\left(-\frac{r^2}{2\sigma_p^2}\right) = \frac{F}{2\pi\sigma_p^2} \exp\left(-\frac{r^2}{2\sigma_p^2}\right) \quad (7)$$

in VOF model, the surface pressure can be expressed as a continuous body forces(CSF) [22] in the vicinity of the interface:

$$F_{arc} = p_a \frac{\rho \nabla F}{\frac{1}{2}(\rho_1 + \rho_2)} \quad (8)$$

where  $P_{\max}$  is maximum arc pressure,  $r$  is effective radius of the arc pressure,  $\sigma_p$  is arc pressure distribution coefficient,  $\nabla F$  is VOF gradient, and  $\rho_1$  and  $\rho_2$  are the density of first and second phases respectively.

Surface tension  $F_{st}$  can be written as follows by CSF method:

$$F_{st} = \gamma \kappa \frac{\rho \nabla F}{\frac{1}{2}(\rho_1 + \rho_2)} \quad (9)$$

where  $\gamma$  is surface tension coefficient,  $\kappa$  is curvature of free surface.

Marangoni shear force acting on metal free surface is given by,

$$\tau_M = \frac{\partial \gamma}{\partial T} \frac{\partial T}{\partial \mathbf{n}} \quad (10)$$

where  $T$  is temperature,  $\mathbf{n}$  is the vector tangential to the local free surface.

The enthalpy- porosity model is employed to process solidification and melting of metals. The liquid fraction is used to implicit track the solid-liquid interface. A momentum source  $F_{ms}$  is added to the momentum equation for representing mushy zone,

$$F_{ms} = \frac{(1-\beta)^2}{(\beta^3 + \varepsilon)} A_{mush} (\mathbf{V} - \mathbf{V}_p) \quad (11)$$

where  $A_{mush}$  is mushy zone constant,  $\beta$  is the liquid volume fraction,  $\varepsilon$  is a small number (0.001) to prevent division by zero,  $\mathbf{V}_p$  is the solid velocity due to the pulling of solidified material out of the domain.

The effects of the plasma arc on the metal surface are represented by an empirical plasma drag force formula [23] to account for the plasma drag effect on the droplet in this study.

$$F_{drag} = C_{ds} \frac{1}{2} \rho_g w_g^2 \left(\frac{\pi D_d^2}{4}\right) \quad (12)$$

where  $C_{ds}$  is the drag coefficient for a sphere,  $\rho_g$  is the plasma gas density;  $w_g$  is the assumed plasma gas velocity, and  $D_d$  is the droplet diameter which determined by wire feed rate  $v_w$ , wire radius  $r_w$ , and droplet transfer frequency  $f_d$  [24],

$$D_d = \left(6r_w^2 \frac{\rho_w v_w}{\rho_d f_d}\right)^{1/3} \quad (13)$$

where  $\rho_w$  and  $\rho_d$  are the mass densities of the electrode and droplet respectively.

The electromagnetic force  $F_{mag}$  in molten pool is assumed to be symmetrical Gaussian distribution. The calculations of current and electromagnetic force are given by Kumar [25].

$$J_z = \frac{Id}{\pi\sigma_j^2} \exp\left(-\frac{r^2 d}{\sigma_j^2}\right) \left(1 - \frac{z}{c}\right) \quad (14)$$

$$J_r = \frac{Id}{2\pi c} \left[1 - \exp\left(-\frac{r^2 d}{\sigma_j^2}\right)\right] \quad (15)$$

$$B_{\theta} = \frac{I\mu_m}{2\pi r} [1 - \exp(-\frac{r^2 d}{\sigma_j^2})] (1 - \frac{z}{c}) \quad (16)$$

$$F_x = -J_z B_{\theta} \frac{x}{r} = -\frac{\mu_m I^2 d}{2\pi^2 \sigma_j^2 r} \exp(-\frac{r^2 d}{\sigma_j^2}) [1 - \exp(-\frac{r^2 d}{\sigma_j^2})] (1 - \frac{z}{c}) \frac{x}{r} \quad (17)$$

$$F_y = -J_z B_{\theta} \frac{y}{r} = -\frac{\mu_m I^2 d}{2\pi^2 \sigma_j^2 r} \exp(-\frac{r^2 d}{\sigma_j^2}) [1 - \exp(-\frac{r^2 d}{\sigma_j^2})] (1 - \frac{z}{c}) \frac{y}{r} \quad (18)$$

$$F_z = J_r B_{\theta} = \frac{\mu_m I^2}{4\pi^2 \sigma_j^2 r} [1 - \exp(-\frac{r^2 d}{\sigma_j^2})]^2 (1 - \frac{z}{c}) \quad (19)$$

In the above equations,  $J_z$  and  $J_r$  are represents the current density in axial and radial direction,  $B_{\theta}$  is magnetic flux density which is induced by welding current.  $I$  is welding current,  $d$  is the current density distribution factor,  $\sigma_j$  is the effective radius of the arc,  $r$  is radius,  $c$  is the thickness of the work piece, and  $\mu_m$  is permeability.  $F_x$ ,  $F_y$  and  $F_z$  are components of electromagnetic force in x, y and z direction.

The external longitudinal static magnetic field can lead to bimodal distribution of current density at molten pool surface [20]. In this paper, the excitation current is 1.1A, and the induction flux density  $B_z$  at metal pool surface is 0.014T (Measured by Gauss meter), comparing with the ref.[19], the changing of welding current density can be ignored. When the external longitudinal static magnetic field is applied, the electromagnetic force can be expressed as,

$$F'_x = F_x + (J_r \times B_z) \frac{x}{r} \quad (20)$$

$$F'_y = F_y + (J_r \times B_z) \frac{y}{r} \quad (21)$$

$$F'_z = F_z \quad (22)$$

### c) Source item of energy

The arc heat  $S_{arc}$  and droplet heat  $S_{drop}$  are the energy input of weld pool. The  $S_{arc}$  can be expressed as a ellipsoid heat source,

$$S_{arc} = q_{arc}(x, y, z) = \frac{3\sqrt{3}\eta(1-\eta_d)UI}{\sigma_q^2 c \pi \sqrt{\pi}} e^{-\frac{3x^2}{\sigma_q^2}} e^{-\frac{3y^2}{\sigma_q^2}} e^{-\frac{3z^2}{c^2}} \quad (23)$$

where  $U$  is welding voltage,  $I$  is welding current,  $c$  is ellipsoid radius of depth direction,  $\eta$  is efficiency of arc thermal,  $\eta_d$  is proportion of droplet energy,  $\sigma_q$  is horizontal axis length of the ellipsoid heat source.

The droplet heat resource  $S_{drop}$  is calculated by means of droplet temperature  $T_d$ . The welding process and numerical model parameters are shown in Table 1.

Table 1 Welding process and numerical model parameters [26]

Parameters	Symbol	Value(unit)
Welding current	$I$	210 A
Welding voltage	$U$	26 V
Welding speed	$v$	460 mm/min
Wire feed rate	$v_w$	3.5 m/min
Gas flow rate	$Q_{gs}$	15 L/min
Excitation current	$I_e$	0/1.1 A
Wire diameter	$D_d$	1.6 mm
Droplet temperature	$T_d$	2500 K
Droplet transfer frequency	$f$	50 Hz
The maximum pressure of arc center	$P_{max}$	468 Pa
Droplet impinging velocity	$v_{\theta}$	0.6 m/s
Welding thermal efficiency	$\eta$	80%
Proportion of droplet energy to welding	$\eta_d$	0.03%

Arc pressure distribution coefficient	$\sigma_p$	3.0 mm
Arc heat flux distribution coefficient	$\sigma_q$	2.6 mm

The thermo-physical properties of mild steel are shown in Table 2.

Table 2 Thermo-physical properties of mild steel

Property	Symbol	Value(unit)
Specific heat of solid phase	$C_s$	700 J/kg.K
Specific heat of liquid phase	$C_l$	780 J/kg.K
Thermal conductivity of solid phase	$k_s$	22 W/m.K
Thermal conductivity of liquid phase	$k_l$	22 W/m.K
Density of solid phase	$\rho_s$	7200 kg/m <sup>3</sup>
Density of liquid phase	$\rho_l$	6950 kg/m <sup>3</sup>
Dynamic viscosity	$\mu$	0.006 kg/m.s
Radiation emissivity	$\varepsilon$	0.4
Boltzmann constant	$\sigma$	$1.3806505 \times 10^{-23}$ J/K
Heat convection coefficient	$h_{con}$	100 W/(m <sup>2</sup> .K)
Latent heat of fusion	$H$	2.47e-5 J/(kg.K)
Solidus temperature	$T_s$	1750 K
Liquidus temperature	$T_l$	1800 K
Ambient temperature	$T_{amb}$	300 K

## 2. Boundary conditions

The CFD codes Fluent is employed to establish the model. The schematic of droplet impingement and dynamics of molten pool simulation are illustrated in Fig. 2. The coordinate system of simulation is locating at top surface of weld bead which is shown in Fig. 1.

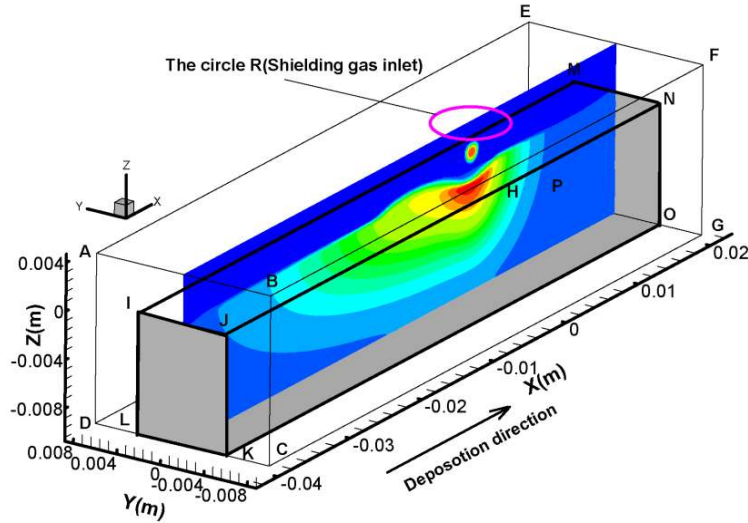


Fig. 2. A schematic representation of GMAW CFD simulation

The domain IJKLMN is metal phase, and the other is air phase. The thermal boundary of metal surface is the combined external heat transfer condition, which can be expressed as following:

$$-k \frac{\partial T}{\partial n} = h_{conv}(T - T_{amb}) + \sigma \varepsilon (T^4 - T_{amb}^4) \quad (24)$$

where  $h_{conv}$  is heat convection coefficient,  $\sigma$  is Boltzmann constant,  $\varepsilon$  is Radiation emissivity, and  $T_{amb}$  is ambient temperature.

The velocity of shield gas is decided by gas flow rate and nozzle diameter, the expression of the velocity can be written as Eq.(22) [27],

$$v_z(r) = \frac{2Q}{\pi} \frac{\left\{ R_n^2 - r^2 + (R_n^2 - R_w^2) \frac{\ln(r/R_n)}{\ln(R_n/R_w)} \right\}}{\left\{ R_n^4 - R_w^4 + \frac{(R_n^2 - R_w^2)^2}{\ln(R_n/R_w)} \right\}} + v_w \frac{\ln \frac{R_n}{r}}{\ln \frac{R_n}{R_w}}, \quad r = \sqrt{x^2 + y^2} \leq R_n \quad (25)$$

where  $Q$  is gas flow rate,  $R_w$  is wire radius,  $R_n$  is nozzle diameter.

The boundary conditions of CFD model are shown in Table 3.

Table 3 Boundary conditions of CFD model

Boundary	Type	$u$ (m/s)	$v$ (m/s)	$w$ (m/s)	$T$ (K)
IJKL	Wall	0	0	0	(24)
MNOP	Wall	0	0	0	(24)
LKOP	Wall	0	0	0	(24)
ABCD(except IJKL)	Pressure outlet	Unspecified	Unspecified	Unspecified	300K
EFGH(except MNOP)	Pressure outlet	Unspecified	Unspecified	Unspecified	300K
DCGH(except LKOP)	Pressure outlet	Unspecified	Unspecified	Unspecified	300K
BCFG	Pressure outlet	Unspecified	Unspecified	Unspecified	300K
AEHD	Pressure outlet	Unspecified	Unspecified	Unspecified	300K
ABFE(except the circle R)	Pressure outlet	Unspecified	Unspecified	Unspecified	300K
The circle R	Velocity inlet	0	0	(25)	300K

### Simulation results and discussion

In current study, 0A and 1.1A excitation current are applied in the coil shown in Fig.1. Fig. 3 represents the distributions of electromagnetic force on the path ( $z=-2\text{mm}$ ,  $y=0$ ,  $x(-10\text{mm}\sim 10\text{mm})$ ), it can be seen that external longitudinal static magnetic field induces the tangential stirring force in molten pool.

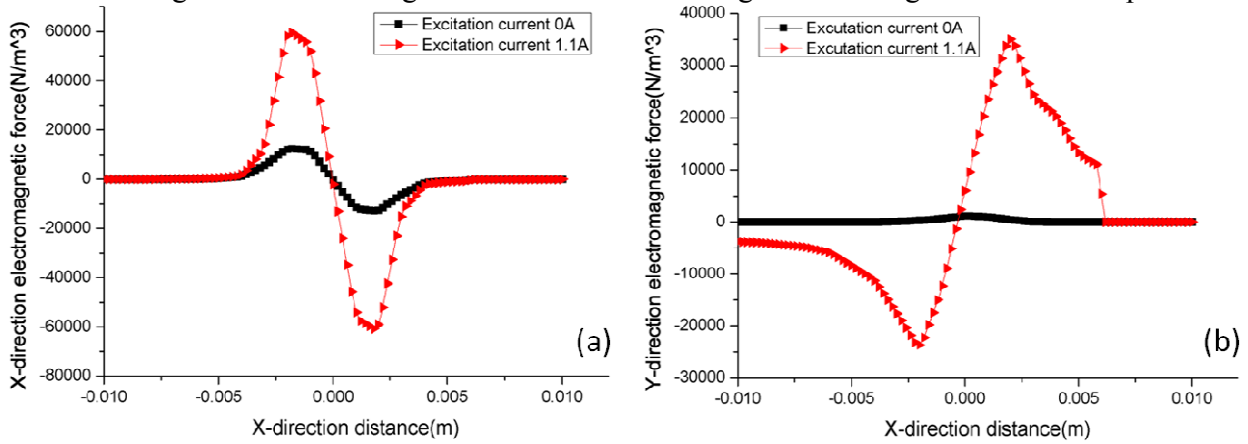
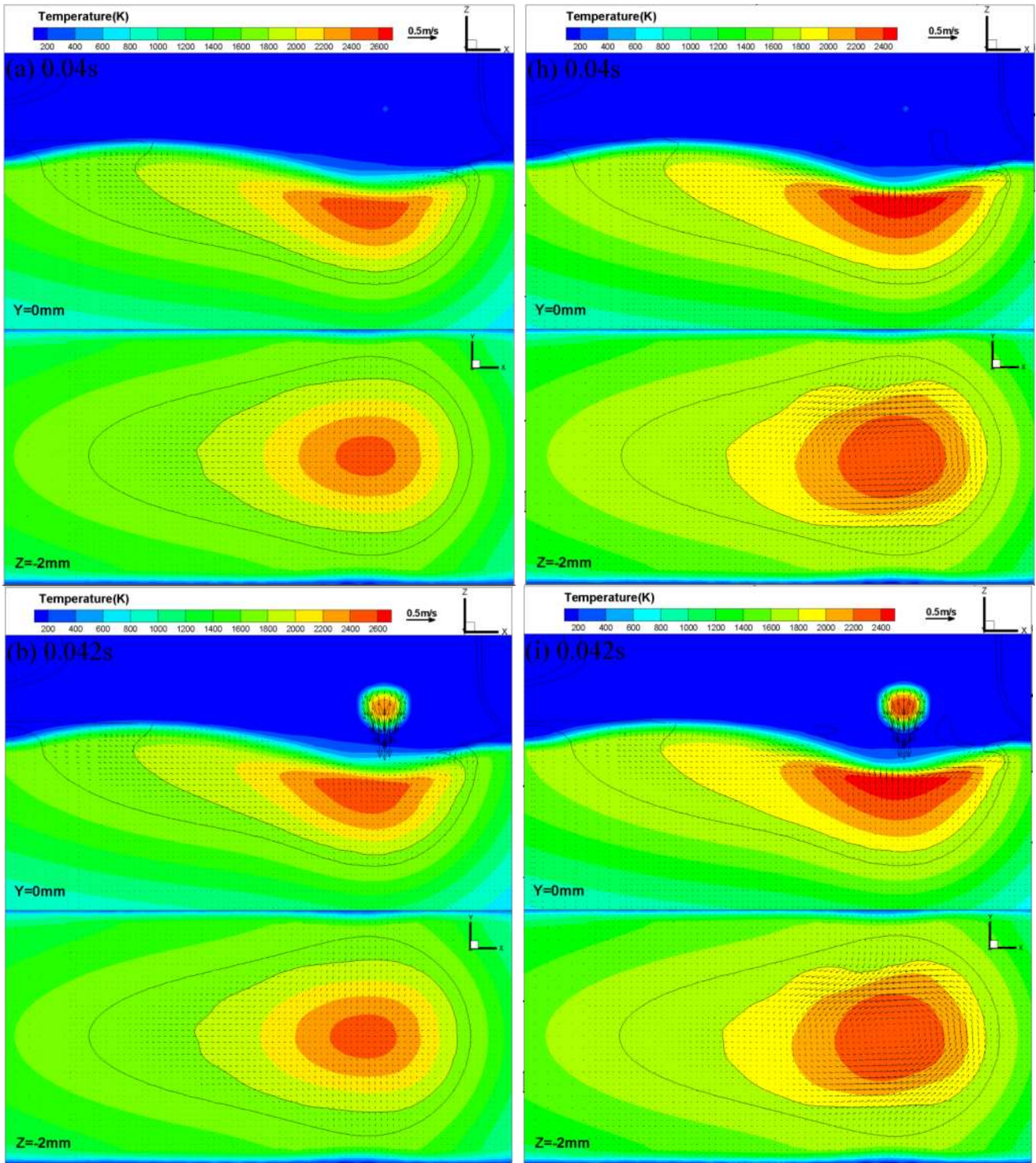


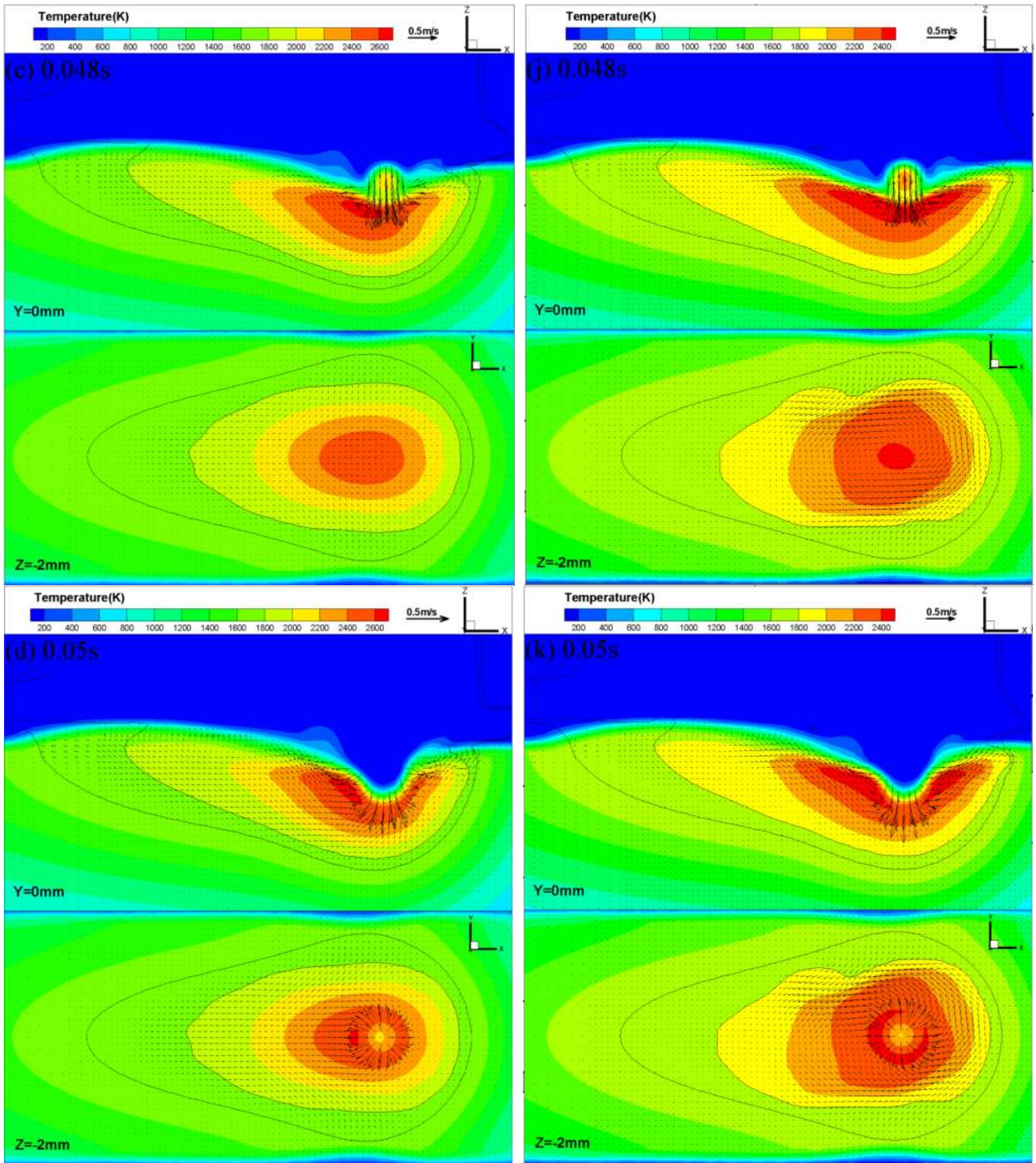
Fig.3. Electromagnetic force evolution on the path ( $z=0$ ,  $y=0$ ,  $x(-10\text{mm}\sim 10\text{mm})$ ). (a) X-direction; (b) Y-direction.

One period of droplet transition has been simulated, and the results of temperature field and velocity vectors are shown in Fig. 4. Fig.4 (a)~(g) and Fig.4 (h)~(n) are the simulated results under the 0A and 1.1A excitation current respectively.

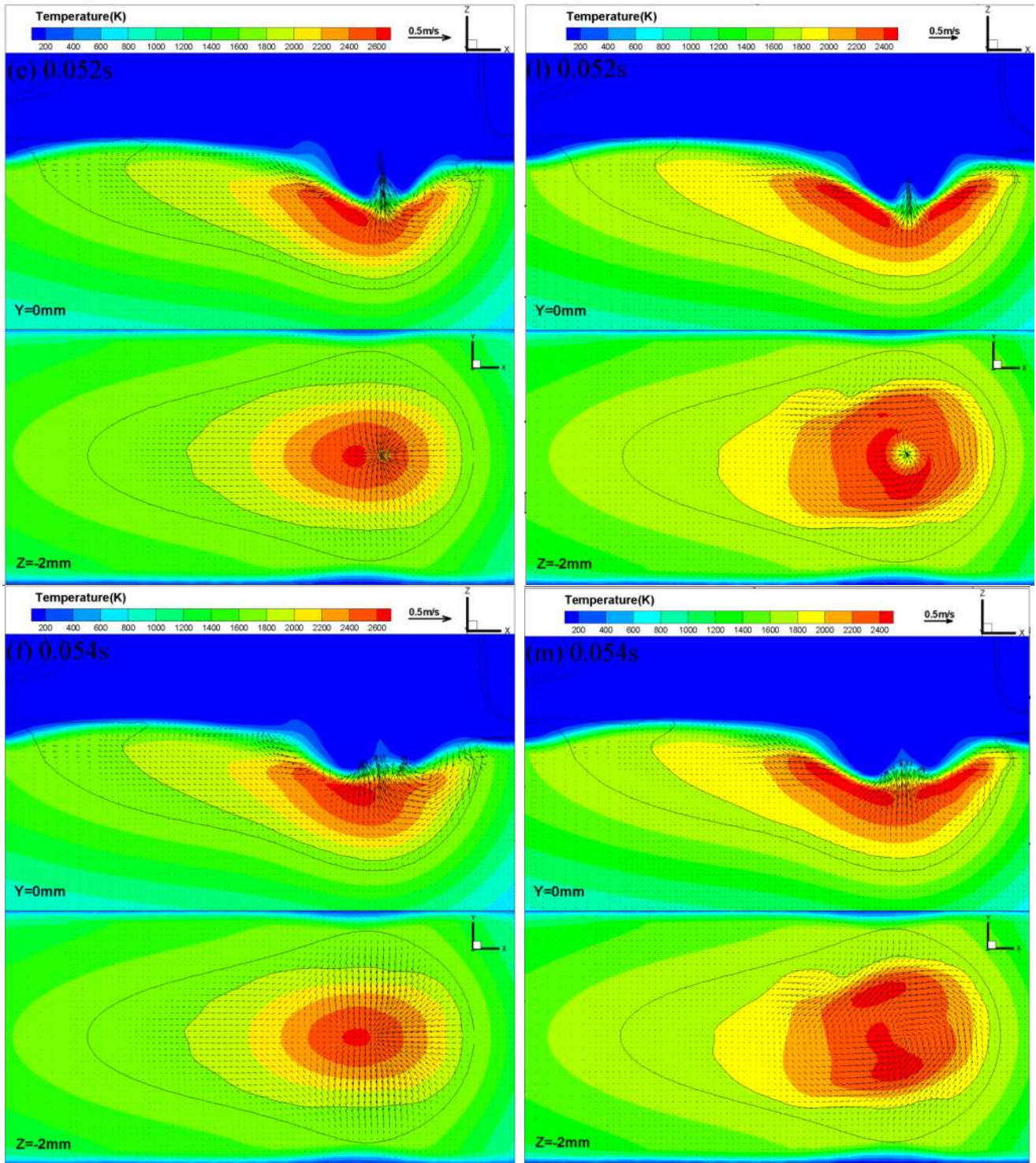












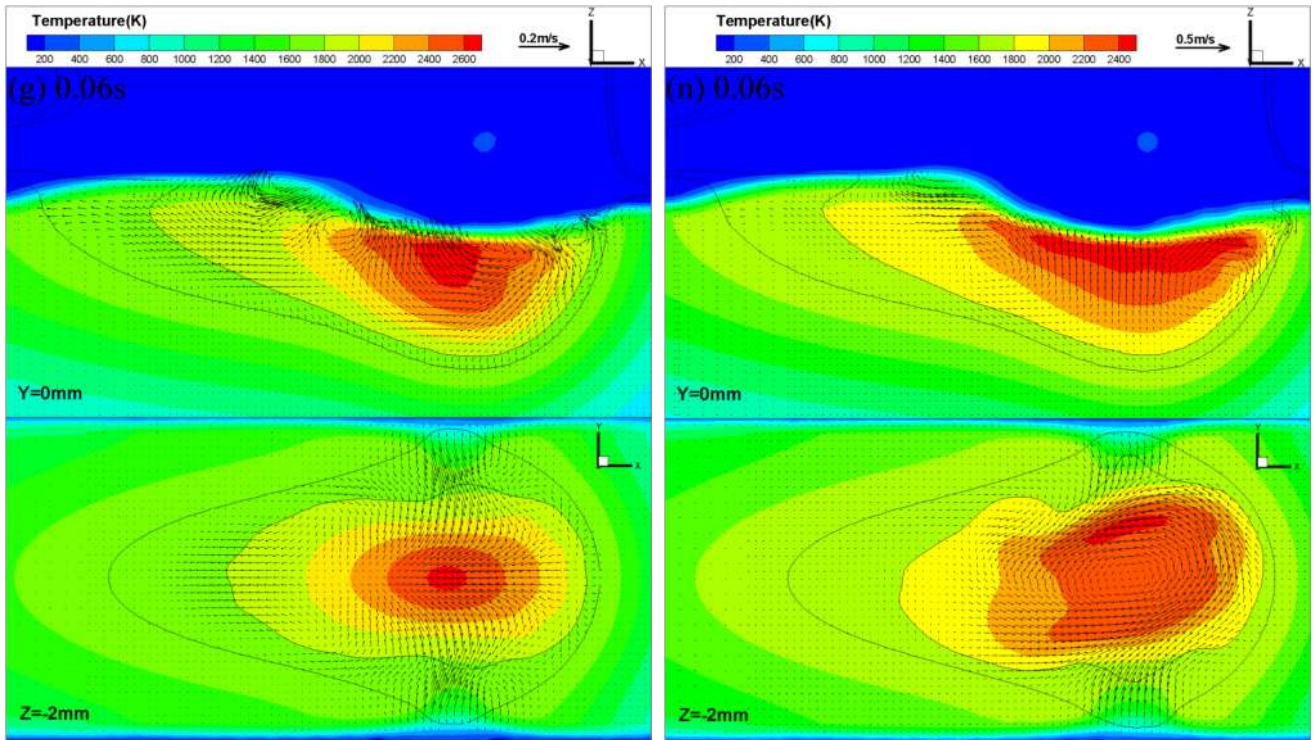


Fig.4. Metal transition and metal pool dynamics analysis results

From Fig. 4, it can be clearly seen that while the longitudinal magnetic field is applied, the flow of molten pool is mainly flowing around the z axis at  $z=-2\text{mm}$  section. More uniform temperature distribution as well as smaller temperature gradient is obtained in the pool as a result of the rotational movement. Simultaneously, the molten pool isotherms become asymmetric distribution. At 0.048s to 0.052s, droplet impingements acting on molten pool are more pronounced when the longitudinal magnetic field is applied. After 0.052s, molten metal began to fall, it can be seen that the molten metal at the rear of molten pool is higher when the longitudinal magnetic field is applied at 0.06s, which can predict that surface ripples on solidified weld bead will be higher than normal deposition.

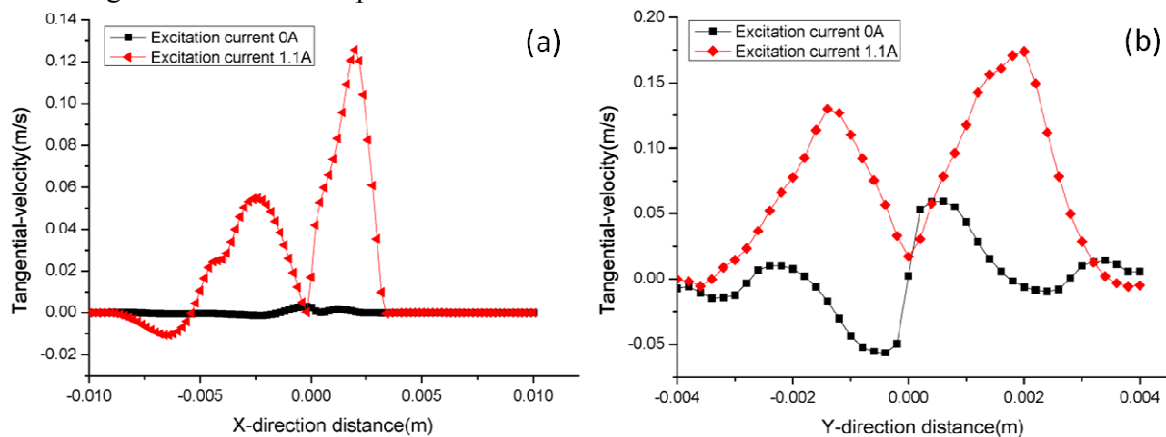


Fig.5. Tangential-velocity evolution on Path1 and Path2 at 0.06s. (a) Path 1; (b) Path 2.

Fig.5 represents the distributions of tangential-velocity on path 1 ( $z=-2\text{mm}$ ,  $y=0$ ,  $x(-10\text{mm}\sim 10\text{mm})$ ) and path 2 ( $z=-2\text{mm}$ ,  $x=0$ ,  $y(-4\text{mm}\sim 4\text{mm})$ ) at 0.06s. It can be seen that the molten pool has a significant tangential velocity while external longitudinal magnetic field is applied. Because of the asymmetry between front and rear of the molten pool, the tangential-velocity is not equal on path 1 at front and rear (shown in Fig.5 (a)). The tangential-velocity on path 2 is substantially equal between left and right of the molten pool (shown in Fig.5 (b)).



It can also be predicted from Fig. 4 and Fig. 5 that, the tangential motion of molten metal will drive the molten metal moving to the edge of the pool and reduce the height of single-bead as well as increase the width. Simultaneously, the smaller temperature gradient is an important factor for small residual stress and distortion in AAM parts [18].

## Experiments

The schematic representation of longitudinal magnetic field assisted AAM is shown in Fig.1, and the schematic diagram of the experimental set-up are shown in Fig.6, the arrows represent the direction of the material flow or information flow.

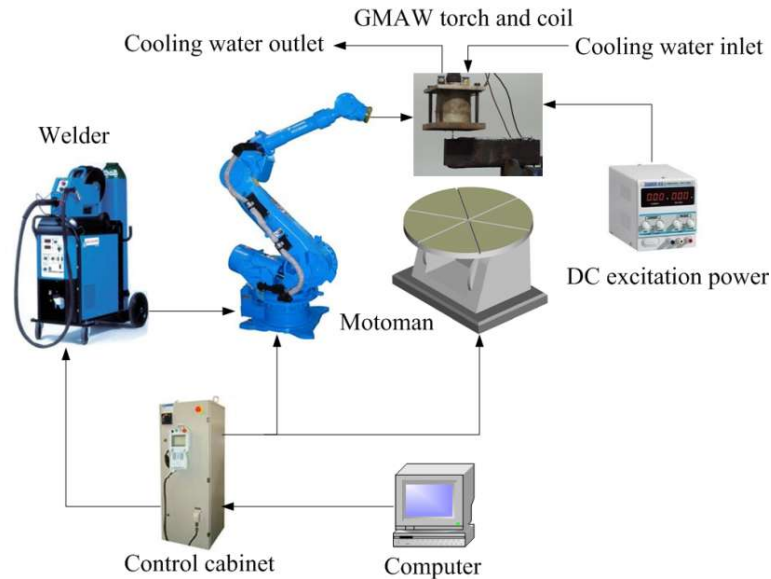


Fig.6. Schematic diagram of the experimental set-up.

The experimental process parameters are shown in Table 4. The welding mode is DC pulse mode which the process parameters include peak voltage( $U_{peak}$ ), base current( $I_{base}$ ), wire feed rate( $V_{wire}$ ), welding speed( $V_{weld}$ ), frequency( $f$ ) and peak pulse time( $T_{pulse}$ ).

Table 4 Experimental process parameters

$U_{peak}$ (V)	$I_{base}$ (A)	$V_{wire}$ (m/min)	$V_{weld}$ (mm/min)	$f$ (Hz)	$T_{pulse}$ (ms)	Excitation current(A)
30	35	7.5	530	230	3.1	1.1

According to ref.3, the ratio of the wire feed rate to the welding speed(RWFRTWS) is more than 12.5 , the cross-section profile can be fitted with an arc curve. The RWFRTWS of current experiment is more than 14, so the optimal center distance of overlapping beads can be calculated by arc curve overlapping mode, the specific calculation methods and formulas can be found in ref.3. Fig.7(a) is the cross section of single weld bead, the left bead is normal deposition bead and the right bead is magnetic field assisted deposition bead. Fig.7(b) and Fig.7(c) are the cross section of one layer and four beads overlapping of normal deposition and magnetic field assisted deposition respectively. The sectional dimensions of weld bead are shown in Table 5. It can be seen that the width of single-bead increased as well as the height of bead decreased significantly when longitudinal static magnetic field was applied. The experimental data are in accordance with the predicted results. The optimal overlapping distance can be calculated and obtained a better overlapping bead morphology [3], however, it is impossible to achieve the ideally at overlapped surface which has been evidenced by experimental study [28, 29]. Compared with the normal deposition overlapping beads, the magnetic field assisted deposition overlapping beads are more flat and uniform and beneficial to stacking deposition for next layer and improving the surface quality and dimensional accuracy of the AAM parts.

Table 5 The sectional dimensions of weld bead

Items	Single weld bead		The width of four beads overlapping deposition(mm)
	Height(mm)	Width(mm)	
Normal deposition	2.5	8	22
Magnetic field assisted deposition	2	10	27

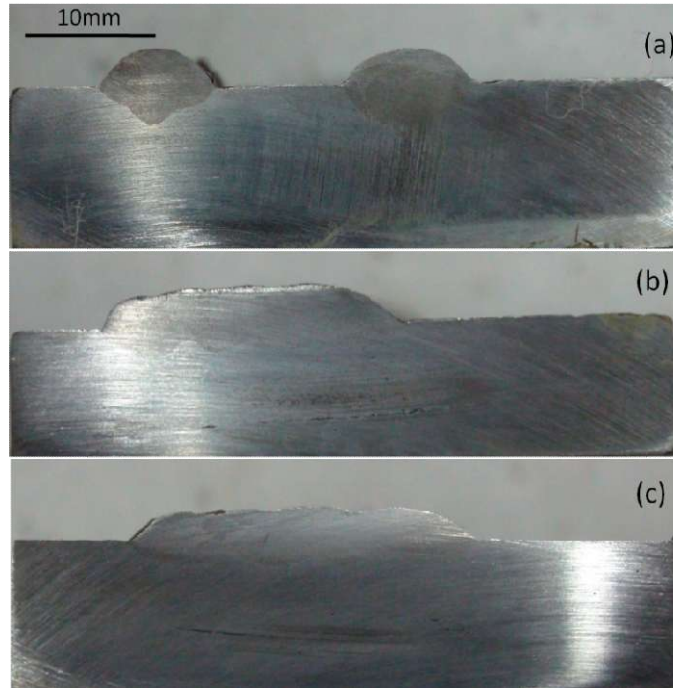


Fig.7. The cross section of single weld bead and overlapping beads. (a) single weld bead; (b) four beads overlapping of normal deposition; (c) four beads overlapping of magnetic field assisted deposition.

### Conclusions

A new arc based additive manufacturing method assisted with external longitudinal static magnetic field is proposed, and the corresponding numerical simulation and experimental investigation for normal deposition and external longitudinal magnetic field assisted deposition are performed. The following main results are gained:

- 1) The external longitudinal static magnetic field can induce the tangential stirring force in molten pool and drive the molten metal moving to the edge of the pool, which can reduce the temperature gradient in forming region.
- 2) The related experimental results show that the tangential stirring force can reduce the height of single-bead as well as increase the width of single-bead. The experimental data are in accordance with the predicted results.
- 3) The external longitudinal magnetic field assisted multi-beads overlapping are more flat and uniform which is beneficial to stacking deposition for next layer and improving the surface quality and dimensional accuracy of the AAM parts.

### References

- [1] Stenbacka N, Choquet I, Hurtig K. Review of arc efficiency values for gas tungsten arc welding[C]//IIW Commission IV-XII-SG212, Intermediate Meeting, BAM, Berlin, Germany, 18-20 April, 2012. 2012: 1-21.

- [2] Sreenathbabu A, Karunakaran K P, Amarnath C. Statistical process design for hybrid adaptive layer manufacturing[J]. Rapid prototyping journal, 2005, 11(4): 235-248.
- [3] Xiong J, Zhang G J, Gao H M, Wu L, Modeling of bead section profile and overlapping beads with experimental validation for robotic GMAW-based rapid manufacturing, Robotics and Computer-Integrated Manufacturing 29 (2013) 417–423.
- [4] Xiong J, Zhang G J. Adaptive control of deposited height in GMAW-based layer additive manufacturing. Journal of Materials Processing Technology 214 (2014) 962– 968.
- [5] Ding D H, Pan Z G, Dominic Cuiuri, Huijun Li. A multi-bead overlapping model for robotic arc based additive manufacturing (WAAM). Robotics and Computer-Integrated Manufacturing 31 (2015) 101–110.
- [6] Malinowski-Brodnicka M, Den Ouden G, Vink W J P. Effect of electromagnetic stirring on GTA welds in austenitic stainless steel[J]. Welding J, 1990, 69(2): 52s-59s.
- [7] Chang Y L, Che X P, He Y Y (2008) Influence of longitudinal magnetic field on metal transfer in MIG arc welding. Chin Weld 17(2):27–31
- [8] Jiang SY, Zheng X F, ChenHM(2004) Outside magnetic field control to spatter of CO2 arc welding. Trans Chin Weld Inst 25(3):65–67
- [9] Luo J, Luo Q, Wang X, et al. EMS-CO2 Welding: A New Approach to Improve Droplet Transfer Characteristics and Welding Formation[J]. Materials and Manufacturing Processes, 2010,25(11):1233-1241.
- [10] Chang Y L, Liu X L, Lu L, et al. Impacts of external longitudinal magnetic field on arc plasma and droplet during short-circuit GMAW[J]. The International Journal of Advanced Manufacturing Technology, 2014, 70(9-12): 1543-1553.
- [11] Ushio M, Wu C S. Mathematical modeling of three-dimensional heat and fluid flow in a moving gas metal arc weld pool[J]. Metallurgical and materials transactions B, 1997, 28(3): 509-516.
- [12] Cao Z, Yang Z, Chen X L. Three-Dimensional Simulation of Transient GMA Weld Pool with Free Surface[J]. SUPPLEMENT TO THE WELDING JOURNAL, 2004,38(6):169-176.
- [13] Hu J, Tsai H L. Heat and mass transfer in gas metal arc welding. Part II: The metal[J]. International Journal of Heat and Mass Transfer, 2007,50(5-6):808-820.
- [14] Rao Z H, Hu J, Liao S M, et al. Modeling of the transport phenomena in GMAW using argon–helium mixtures. Part II-The metal[J]. International Journal of Heat and Mass Transfer, 2010,53(25-26):5722-5732.
- [15] Hu J, Guo H, Tsai H L. Weld pool dynamics and the formation of ripples in 3D gas metal arc welding[J]. International Journal of Heat and Mass Transfer, 2008,51(9-10):2537-2552.
- [16] Rao Z H, Zhou J, Liao S M, et al. Three-dimensional modeling of transport phenomena and their effect on the formation of ripples in gas metal arc welding[J]. Journal of Applied Physics, 2010, 107(5): 054905.
- [17] Chang Y L, Lu L, Liu X L, et al. Numerical Simulation of SAW Heat Source in the External Longitudinal Magnetic Field in 16Mn Steel[J]. Materials Science Forum, 2013,762:584-589.

- [18] Bai X W, Zhang H, Wang G, Modeling of the moving induction heating used as secondary heat source in weld-based additive manufacturing, *The International Journal of Advanced Manufacturing Technology*, 2015, Volume 77, Issue 1-4, pp 717-727.
- [19] Luo J, Luo Q, Lin Y H, Xue J, A New Approach for Fluid Flow Model in Gas Tungsten Arc Weld Pool Using Longitudinal Electromagnetic Control, *Welding Journal* 2003, 82 (8), 202–206
- [20] Yin X, Gou J, Zhang J, et al. Numerical study of arc plasmas and weld pools for GTAW with applied axial magnetic fields[J]. *Journal of Physics D: Applied Physics*, 2012, 45(28): 285203.
- [21] Zhang W. Heat and fluid flow in complex joints during gas metal arc welding—Part I: Numerical model of fillet welding [J]. *J Appl Phys*, 2004, 95(9): 5210.
- [22] Brackbill J, Kothe DB, Zemach C. A continuum method for modeling surface tension[J]. *Journal of computational physics*, 1992, 100(2): 335-354.
- [23] Xu G, Hu J, Tsai H L. Three-dimensional modeling of arc plasma and metal transfer in gas metal arc welding[J]. *International Journal of Heat and Mass Transfer*, 2009, 52(7): 1709-1724. Xu G, Hu J, Tsai H L. Three-dimensional modeling of arc plasma and metal transfer in gas metal arc welding[J]. *International Journal of Heat and Mass Transfer*, 2009, 52(7): 1709-1724.
- [24] Murphy A B. Influence of droplets in gas-metal arc welding: new modelling approach, and application to welding of aluminium[J]. *Science and Technology of Welding and Joining*, 2013, 18(1): 32-37.
- [25] Kumar A, DebRoy T. Calculation of three-dimensional electromagnetic force field during arc welding[J]. *Journal of Applied Physics*, 2003,94(2):1267.
- [26] Rao Z H, Zhou J, Liao S M, et al. Three-dimensional modeling of transport phenomena and their effect on the formation of ripples in gas metal arc welding[J]. *Journal of Applied Physics*, 2010,107(5):54905.
- [27] Hu J, Tsai H L. Heat and mass transfer in gas metal arc welding. Part I: The arc[J]. *International Journal of Heat and Mass Transfer*, 2007,50(5-6):833-846.
- [28] Suryakumar S, Karunakaran KP, Bernard A, Chandrasekhar U, Raghavender N, Sharma D. Weld bead modeling and process optimization in hybrid layered manufacturing. *Comput-Aided Des*, 2011;43:331–44.
- [29] Aiyiti W, Zhao W, Lu B, Tang Y. Investigation of the overlapping parameters of MPAW-based rapid prototyping. *Rapid Prototyp J*, 2006;12:165–72.